Physics of the Earth and Planetary Interiors 183 (2010) 387–397

Contents lists available at ScienceDirect

Physics of the Earth and Planetary Interiors

journal homepage: www.elsevier.com/locate/pepi

The magnetism of micro-sized hematite explained

Qingsong Liu [a,*], Vidal Barrón [b], José Torrent [b], Huafeng Qin [a], Yongjae Yu [c]

[a] State Key Laboratory of Lithospheric Evolution, Institute of Geology and Geophysics, Chinese Academy of Sciences, 100029 Beijing, China
[b] Departamento de Ciencias y Recursos Agrícolas y Forestales, Universidad de Córdoba, Edificio C4, Campus de Rabanales, 14071 Córdoba, Spain
[c] Department of Geology and Earth Environmental Sciences, Chungnam National University, Daejeon 305-764, Republic of Korea

ARTICLE INFO

Article history:
Received 24 March 2010
Received in revised form 5 August 2010
Accepted 17 August 2010

Edited by: K. Zhang.

Key words:
Hematite
Magnetism
Morphology
Coercivity
Morin transition

ABSTRACT

Several sets of micro-sized synthetic hematite samples were systematically studied by infrared absorption spectroscopy, X-ray diffraction, thermogravimetric and low-temperature magnetic analysis. These hematite samples could be divided into three distinctive morphologies of pseudocubic ($G_{\perp} > 0.17$, the shape factor), platy, and rhombohedral (both $G_{\perp} < 0.14$). Pseudocubic hematite contains more vacancies than other morphologies due to the presence of OH in the crystal. Accordingly, the pseudocubic hematite exhibits a wider Morin transition and higher magnetic coercivity. Both the low temperature changes in coercivity and first-order reversal curve indicate that the pseudocubic hematite is dominated by a combination of magnetocrystalline and magnetoelastic anisotropies. In contrast, because of the low vacancy content, hematite with non-pseudocubic morphologies is governed primarily by the magnetocrystalline anisotropy. Such a simple morphology dependence successfully links microstructure to the bulk magnetic properties of micron-sized hematite and hence improve our understanding of the magnetism of hematite and its possible application in elucidating the origin of hematite in natural environments.

1. Introduction

As an end-member of solid solution series [xFeTiO$_3$, $(1-x)$Fe$_2$O$_3$], hematite (α-Fe$_2$O$_3$) is ubiquitous in various terrestrial environments (Schwertmann and Taylor, 1977). Its contribution as a magnetic remanence carrier is important both on terrestrial lithosphere (Tauxe and Kent, 1984) and possibly on Martian crust (Kletetschka et al., 2000; Dunlop and Kletetschka, 2001) with two interesting features. First, hematite is an antiferromagnetic mineral that can carry stable natural remanent magnetization (NRM), a necessary requirement for the successful paleomagnetic studies. Because of low saturation magnetization (~2.5 A/m), the threshold between single-domain (SD) and pseudo-single-domain (PSD) hematite could be as large as ~20 μm (Kletetschka and Wasilewski, 2002), yet its SD/superparamagnetic (SP) threshold is comparable to that of magnetite (~20 nm) (Banerjee, 1971). Therefore, in natural environments, hematite is often located in a stable SD region, and can thus be one of the most stable NRM carriers. Second, environmental factors strongly influence the formation and preservation of hematite in nature. For example, the hematite (together with goethite, α-FeOOH) content has been widely used as an aeolian contribution in marine and lake sediments (Thompson and Oldfield, 1986; Yamazaki and Ioka, 1997; Maher and Dennis, 2001; Larrasoaña et al., 2003, 2006). In addition, hematite has broader applications from magnetic storage devices to magnetic imaging (Zhao et al., 2007 and references therein).

Magnetic properties of hematite are controlled by many chemical/physical factors such as the grain size (Kletetschka and Wasilewski, 2002), the remanence acquisition temperatures (Flanders and Schuele, 1964; Özdemir and Dunlop, 2005, 2006), the effect of annealing (Zysler et al., 2001), cation substitution (Wells et al., 1999; de Grave et al., 1982, 1983; Liu et al., 2007) and the grain morphology (Iglesias and Serna, 1985; Zhao et al., 2007), and the influence of mineral transformation (Prasada et al., 2006). Such diverse data came from hematites of various origins and grain dimensions including an ideal synthetic single crystal (Sunagawa and Flanders, 1965; Özdemir and Dunlop, 2005), a nano-sized synthetic material (Liu et al., 2007), synthetic coarse-grained multidomain (MD) (Kletetschka and Wasilewski, 2002), and natural hematite particles (Pastrana and Hopstock, 1977; Dankers, 1981; Dekkers and Linssen, 1989; de Boer and Dekkers, 1998; Özdemir et al., 2002). Considering its stability and ubiquity, fine-grained hematite would be important to unravel the lithospheric evolution of the planetary environment. Yet, the magnetic properties of micron-sized synthetic hematite with different morphologies have not been thoroughly examined.

In the present study, we focus on hydrothermally-produced micron-sized hematites of different morphologies. An integrated rock magnetic investigation with additional chemical analysis has

* Corresponding author.
E-mail addresses: liux0272@yahoo.com, qsliu@mail.iggcas.ac.cn (Q. Liu).

0031-9201/$ – see front matter © 2010 Elsevier B.V. All rights reserved.
doi:10.1016/j.pepi.2010.08.008

Table 1
Methods used to synthesize the hematite samples.

Sample	Starting reagents/products	Aging condition	Aging temperature	Time	Reference
H3, H33, K2	(0.019 M $FeCl_3$ + 1.2 × 10^{-3} M HCl) in the same volume of ethanol		90 °C	14 days	Hamada and Matijević (1982)
J12	40 mL 2 M $FeCl_3$ + 40 mL 8 M NaOH		180 °C	2 h	Sugimoto et al. (1993)
H180	Ferrihydrite	5 M NaOH	180 °C	2 h	Sugimoto et al. (1993)
L3	Ferrihydrite	5 M NaOH	70 °C	8 days	Schwertmann and Cornell (2000)
S7, S8	Ferrihydrite	5 M NaOH	70 °C	44 days	Torrent and Schwertmann (1987)

been conducted to determine the effect of morphology, OH incorporation, and vacancies on the magnetic properties of hematite.

2. Samples and methods

The synthesis procedures for the eight studied hematite samples (H3, H33, K2, J12, H180, L3, S7, and S8) are summarized in Table 1. Samples (H180, L3, S7, and S8) that were prepared by aging ferrihydrite in 5 M NaOH, ferrihydrite was precipitated by neutralizing a $Fe(NO_3)_3$ solution with NaOH, and polypropylene rather than glass bottles were used to prevent contamination from silica. In all cases, reagent grade chemicals were used. After synthesis, the hematite suspensions were centrifuged, and washed with de-ionized water several times to remove soluble salts and either dried in an oven at ~110 °C or freeze dried. The content of Fe in the samples was determined in duplicate by dissolving the sample in hot 6 M HCl and analyzing Fe in solution by atomic absorption spectrometry. The coefficient of variation of this method is <2%.

The infrared (IR) absorption spectra of the samples were recorded from KBr disks using a Bruker Tensor 27 MIR spectrophotometer with a precision better than 1 cm^{-1}. The X-ray diffraction (XRD) patterns were measured using a Siemens D5000 X-ray diffractometer with a sealed tube and monochromatic Co$K\alpha$ radiation at a scan speed of 0.005° 2θ s^{-1}. The proportion of goethite in samples containing it was estimated by Rietveld refinement using the POWDER CELL software (Kraus and Nolze, 1996).

Scanning electron microscope (SEM) observations were made using a LEO 1450VP SEM, operated at 10–20 keV with an acceleration voltage of 17–20 pA. The thermogravimetric analysis was made on a Setaram instrument using about 25 mg samples, from 25 and 1000 °C with a heating rate of 5 °C/min.

First-order reversal curve (FORC) analyses were made using a Princeton Measurements Corporation vibrating sample magnetometer (Micromag VSM 3900) at room temperature (300 K) and low temperature (25 K or 50 K). For each sample, 140 FORCs were measured with an averaging time of 250 ms and a wait time of 250 ms between successive measurements. A smoothing factor of 5 (SF = 5) was used to attenuate effects from measurements errors.

Cycling of saturation isothermal remanent magnetization (SIRM) is indicative of magnetic mineralogy and granulometry. Thus, a low-temperature cycling (LTC) of room-temperature produced SIRM in a zero-field condition was monitored using a Quantum Design Magnetic Property Measurement System (MPMS). First, at 300 K, a saturation remanence magnetization ($SIRM_{300\,K}$) was imparted in a field of 5 T. The measurements of $SIRM_{300\,K}$ were cycled from 300 K to 10 K and then from 10 K to 300 K in a zero field. The ambient field in the sample chamber is ~50 μT, which does not contribute significantly to the net measured magnetization. Second, after the first run, the same samples were further cooled down to 10 K, where a magnetic field of 5 T was applied ($SIRM_{10\,K}$), then the field was turned off, and the samples were measured on warming to 300 K in a zero field. The temperature sweeping rate is 5 K/min, and the temperature interval is 2 K.

Temperature dependence of magnetic hysteresis was also performed using the MPMS. For the measurements of hysteresis loops, the maximum applied field is set to 5 T. The coercivity (B_c) and saturation remanence magnetization (M_{rs}) are obtained without correcting the high-field slope. Hysteresis loops were measured at representative temperatures whenever SIRM showed meaningful variations. For H33, hysteresis loops were measured at 300, 275, 250, 230, 215, 200, 180, 150, 125, 100, 80, and 50 K, respectively. For J12, loops were made at 300, 250, 230, 215, 200, 180, 150, 100, and 50 K, respectively.

3. Results

3.1. Chemical properties and XRD and SEM data

The main physical, chemical and magnetic properties of the samples are shown in Table 2. The XRD results (Fig. 1 and Table 2) indicate that all samples are dominated by hematite, goethite being present in small proportion only in J12, L3, and S8. The ratio between the intensities of (1 1 0) and (1 0 4) reflections (which pertain to a plane parallel to the *c*-axis and to a near-basal plane, respectively) (Barrón et al., 1988) ranges widely (0.33–0.68; Table 2). These differences can be caused by vacancies or preferential orientation, which can in turn be related to differences in

Table 2
Summary of properties of the studied hematite samples[a].

Type	Sample	Goethite (%)	Fe (%)	Water loss[b] (%)	B_c (mT)	B_{cr} (mT)	M_s (Am^2 kg^{-1})	Intensity ratio[c], peak at (1 1 0)/peak at (1 0 4)	$G_\perp$	R_{SIRM}	Grain size[d] (μm)
Pseudocubic	H3	0	68	3.2	606.6	739.9	0.079	0.68	0.19	0.94	2.1 ± 0.3
	H33	0	68.5	2.4	553.9	681.2	0.084	0.65	0.17	0.91	2.4 ± 0.5
	K2	0	69	2.0	545.9	628.4	0.032	0.60	0.19	0.76	1.5 ± 0.6
Rhombohedral	J12	7	68.5	2.1	36.3	270.7	1.959	0.54	0.06	0.42	2.1 ± 0.6
Platy	H180	0	70	0.7	107.5	189.6	0.177	0.56	0.13	0.32	1.5 ± 0.3
	L3	2	69.5	0.7	221.7	293.4	0.209	0.53	0.13	0.38	2.6 ± 1.0
	S7	0	69.5	1.3	86.3	251.1	0.730	0.38	0.05	0.22	2.3 ± 0.7
	S8	4	69	1.9	67.6	236.6	0.603	0.33	0.05	0.35	4.8 ± 1.2

[a] Abbreviations: B_c, coercivity; B_{cr}, remanence coercivity; M_s, saturation magnetization; $G_\perp$, shape factor from the IR spectrum; R_{SIRM}, memory ratio of isothermal remanent magnetization.
[b] Water loss between 25 °C and 1000 °C corrected for water in goethite.
[c] From the 1 1 0 and 1 0 4 reflections of the X-ray diffraction pattern.
[d] The grain size was statistically determined by counting ~100 particles for each sample.

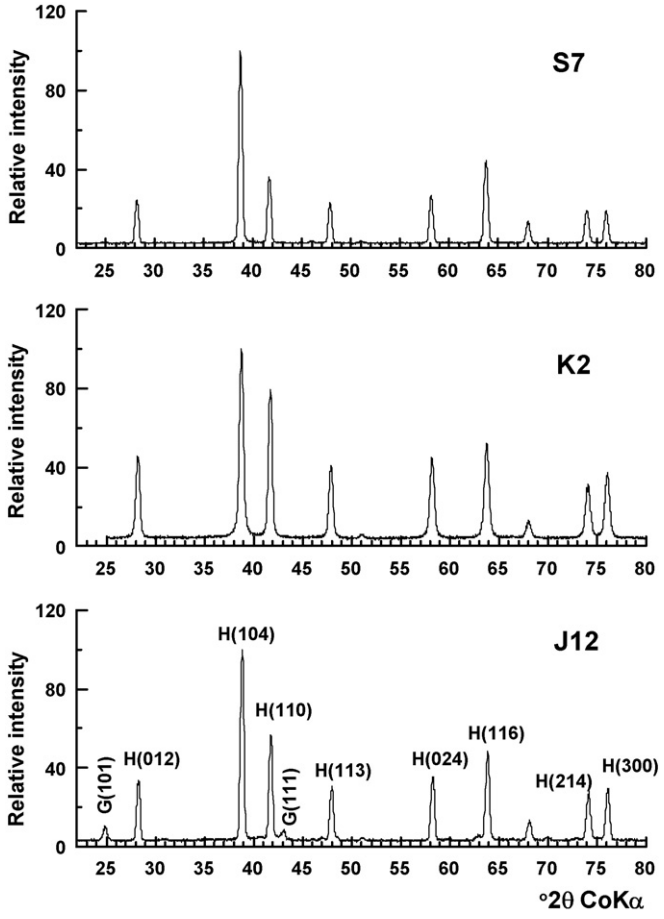

Fig. 1. X-ray diffraction patterns of two pure hematites (K2, S7) and a hematite with goethite (J12).

crystal morphology (Table 2). Because the Fe contents of the different samples are virtually identical (68–70%; Table 2) and close to stoichiometric hematite (70%), we assume that the influence of vacancies is small relative to that of preferential orientation. Indeed the samples with platy morphology exhibit ratios significantly lower than those of the pseudocubics (0.33–0.56 and 0.60–0.68, respectively), the rhombohedral morphology exhibiting an intermediate value (0.54). This is consistent with the fact that the platy hematite particles lie on a basal (0 0 1) or near basal (e.g. 1 0 4) plane on the pressed powder mount used to acquire the X-ray diffraction pattern.

According to intensive SEM observation, morphologies of hematite samples used in this study are classified into three types: pseudocubic (H3, H33, and K2), platy (H180, L3, S7, and S8), and rhombohedral (J12). These hematites have a narrow uniform grain distribution of 1–3 μm. Sample S8 have the coarsest grain size of ~5 μm (Fig. 2).

3.2. IR absorption spectra

Because the frequency of the absorbed IR radiation depends on the rotational energy levels and the force constants of the interatomic bonds, the IR absorption spectra are useful means of identifying and characterizing Fe oxides. As can be seen in Fig. 3, the IR spectra are strongly dependent on the morphology of hematite. This is general phenomenon occurring when particles are smaller than the wavelength of the IR radiation (Van de Hulst, 1957). Specifically, the positions of the IR maxima depend on the shape factor, G, of the hematite particles (Iglesias and Serna, 1985). For an ellipsoid with a, b and c orthogonal semiaxes, $G1 + G2 + G3 = 1$; for a revolution ellipsoid, two of the axial ratios are equal and $G_{//} + 2G_{\perp} = 1$, where $G_{\perp}$ and $G_{//}$ are the shape factors perpendicular to and parallel to the c-axis, respectively. For an oblate revolution ellipsoid, $G_{\perp}$ increases when the $(a = b)/c$ axial ratio decreases (Van de Hulst, 1957).

The pseudocubic hematites exhibit a relatively simple pattern, with four dominant peaks at 300, 410, 510, and 700 cm^{-1} (Fig. 3a). In contrast, the platy and rhombohedral samples show more complicated behaviour, with a subdivision of a dominant 410 cm^{-1} peak into two sub-peaks of smaller wavenumbers and an addition of a new hump or saddle point around 600 cm^{-1} (Fig. 3b). Such a contrasting feature in IR spectra has been attributed to the presence of a hydrohematite as suggested by Wolska (1981). For the hematites studied here, the $G_{\perp}$ values estimated from the calibration curve presented by Iglesias and Serna (1985) range from 0.05 for two platy hematites (S7, S8) to 0.19 for two pseudocubic hematites (H3, K2), consistent with the actual SEM observations (Fig. 2). In general terms, and on the basis of shape factor, the samples could be classified into two groups: pseudocubic with $G_{\perp} > 0.17$ and non-pseudocubic with $G_{\perp} < 0.14$ (Table 2). Barrón et al. (1984) further showed that Al-for-Fe substitution can also affect the shape factor, although this explanation cannot be invoked for our samples.

3.3. Thermogravimetric analysis

The weight loss between 25 °C and 1000 °C is due to adsorbed water, structural OH and also to the dehydroxylation of goethite in those samples containing it. The thermogravimetric curves for pseudocubic (H3, H33, and K2) and platy and rhombohedral (H180, L3, S7, S8, and J12) hematites are shown in Fig. 4a and b, respectively. As expected, a distinct step at ~300 °C is observed for samples containing goethite (L3, S8, J12). This feature is clearly enhanced in the first derivative of the thermogravimetric curve: a clear minimum is observed, for instance, for J12, the sample with 7% goethite (Fig. 4d), whereas no minimum appears for K2, a goethite-free sample (Fig. 4c).

The water loss between 25 °C and 1000 °C corrected for the loss due to the dehydroxylation of goethite (based the goethite content of the samples and stoichiometric goethite with 10% water) is shown in Table 2. The loss of water was greater for pseudocubic than for platy samples (2.0–3.2% and 0.7–1.9%, respectively), the rhombohedral sample (J12) exhibiting an intermediate value (2.1%). Therefore, the pseudocubic hematites seem to incorporate more structural OH than their platy and rhombohedral counterparts.

3.4. Temperature dependence of high-field remanence

Low-temperature cycling (LTC) of room-temperature SIRM showed irreversible heating and cooling curves (Fig. 5). For the pseudocubic samples (H3, H33, and K2), the remanence gradually decreases upon cooling, and then remains essentially stable below ~60 K. The gradual increases in remanences upon heating are due to the remanence memory. Apparently, after a complete LTC cycle, the initial IRM has been partially demagnetized.

For the platy (S7, S8, H180, L3) and rhombohedral (J12) samples, a clear Morin transition is observed around 220 K, which is lower than the reference value of 250 K for the neatly pure hematite (Muench et al., 1985). In addition, >50% of the initial remanence has been demagnetized in these samples. For J12, L3, and S8, a gradual increase of SIRM upon cooling below 200 K was observed resulting from the increase in M_s of goethite.

For comparison, the warming curves for the IRM acquired at 10 K (IRM_{10K}) are also shown in Fig. 5. Overall, they exhibit patterns similar to the corresponding LTC warming cures. Özdemir

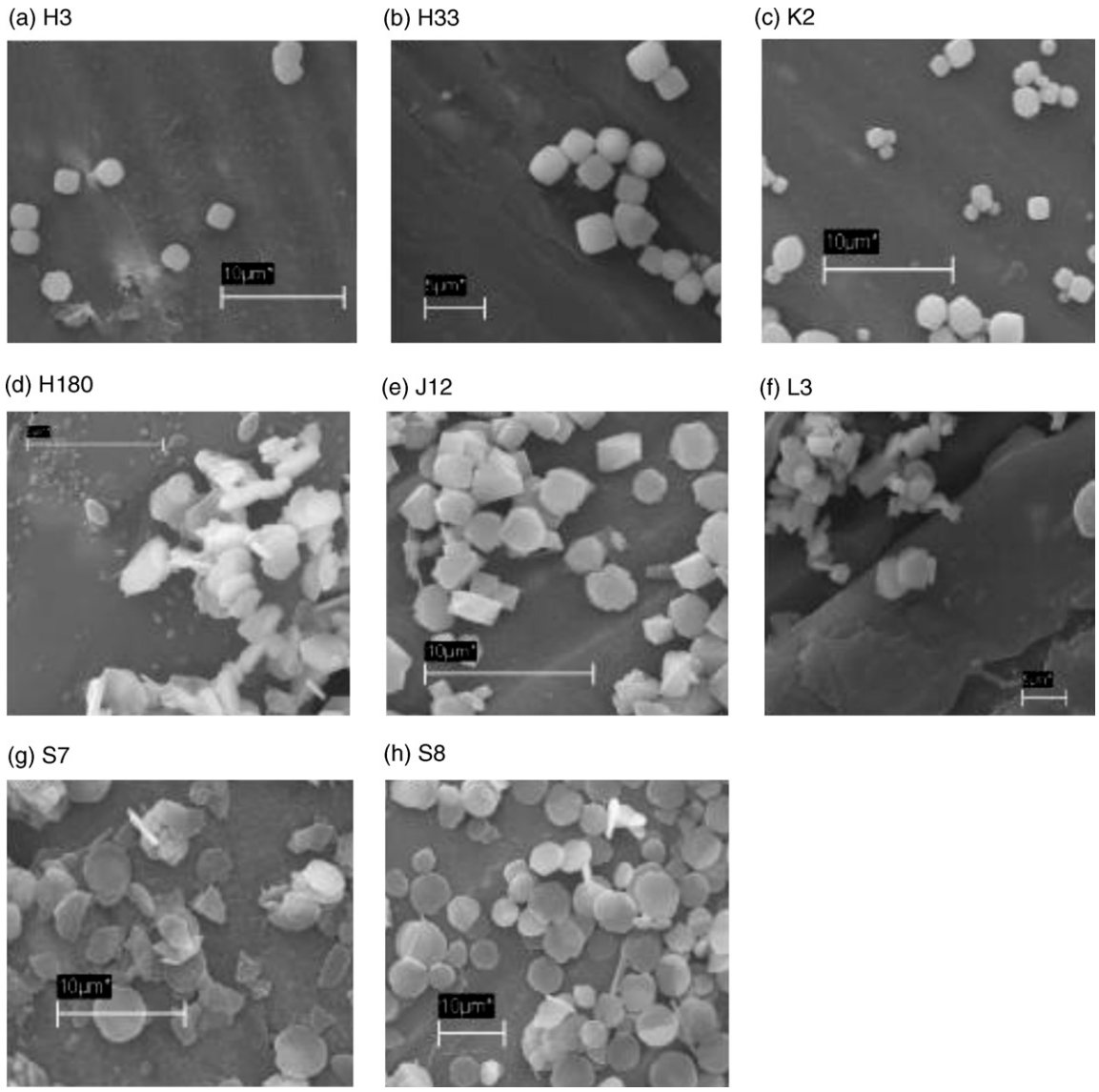

Fig. 2. SEM observation showing the morphologies of hematite samples examined in this study. The scale bar is 5 μm for samples H33 (b), H180 (d) and L3 (f), and is 10 μm for the others.

and Dunlop (2006) demonstrated that the IRM acquired below the Morin transition is caused solely by the defect remanence (uncompensated spins). By comparing the similarity between the warming of $IRM_{10\,K}$ and the cooling of $SIRM_{300\,K}$, a dominance of defect versus canted remanent magnetization can be evaluated. The warming of $IRM_{10\,K}$ and the cooling of $SIRM_{300\,K}$ are nearly identical for non-pseudocubic hematites, suggesting that the defect remanence is dominating (Fig. 5). On the other hand, a noticeable offset between the warming of $IRM_{10\,K}$ and the cooling of $SIRM_{300\,K}$ is observed for pseudocubic hematites, indicating that both defect and canted mechanisms contribute to the magnetic remanence (Fig. 5).

3.5. Temperature dependence of hysteresis loops

At 300 K, pseudocubic samples tend to have larger coercivity but lower M_s than the platy and rhombohedral samples (Table 2). Temperature dependence of magnetic hysteresis is useful in unravelling the dominance of magnetic or other physical anisotropy. A typical example of temperature-dependent hysteresis variation is shown in Fig. 6. For H33 (pseudocubic), at 300 K, the loop became closed at about 1.5 T. (Fig. 6). With decreasing temperatures, the saturation was achieved at higher fields (~2.6 T at 100 K and >3 T at 50 K). Distinctively different hysteresis properties with a low coercivity are observed for J12 (rhombohedral). For J12, hysteresis loops are not saturated even at 3 T (Fig. 6).

Temperature dependence of magnetic coercivity and saturation remanent magnetization for H33 and J12 is displayed in Fig. 7. For H33, coercivity increased from 300 K to 250 K with an exception at 210 K. Below 180 K, coercivity decreased with cooling to 100 K (Fig. 7a). Temperature dependence of M_{rs} for H33 mimics the cycling of $IRM_{300\,K}$ where broad unblocking was monitored between ~220 K and 80 K (Fig. 7b). In contrast, for J12 (rhombohedral), both the B_c and M_{rs} decrease sharply between 250 K and 200 K (Fig. 7c and d).

3.6. FORC diagram

In addition to a conventional hysteresis characterization, FORC analysis was carried out to visualize the distribution of magnetic coercivities. As in hysteresis observation, pseudocubic hematites (H33 and K2) showed much higher coercivities than other morphologies (S8, L3 and J12) (Fig. 8). At low temperatures, the centers of the peak FORC distributions (CPFD) tends to be larger for pseu-

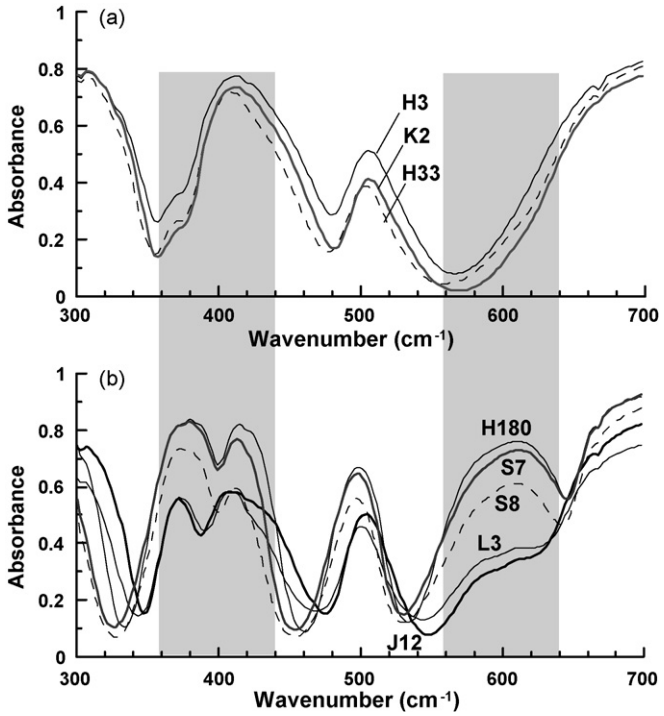

Fig. 3. The IR spectra for the studied hematite samples. (a) Pseudocubic, and (b) platy and rhombohedral. The grey regions are used to distinguish the differences in the major absorbance peaks around 400 and 600 cm^{-1}.

docubic samples (H33 and K2) but smaller for platy samples (S8, L3 and J12). For all occasions, CPFD is located below the central symmetric line.

4. Discussion

4.1. Effects of the OH groups on the magnetic properties of hematite

As a non-destructive technique, low-temperature magnetic analysis has been widely used to identify the magnetic phases. Magnetite sharply changes its properties at the Verwey transition (T_V at ~120 K), where it changes from pseudocubic to monoclinic crystalline symmetry (Verwey, 1939). In contrast, the Morin transition (T_M, at ~250 K) for hematite corresponds only to its isotropic point, where its anisotropy constant changes the sign, leading to the sublattice spins switch from the basal plane above T_M to the *c*-axis below it.

Previous studies showed that T_M is affected by multiple factors, including the particle size, morphology, and impurities. For spherical hematites, T_M will gradually decrease with decreasing grain sizes, and almost disappear in a grain with diameter <10–20 nm, which can be accounted for by a lattice expansion in a small particle (Bando et al., 1965; Ayyub et al., 1988). Presence of impurities or vacancies, accumulation of strain, and crystal defects can also reduce T_M (Morin, 1950; Flanders and Remeika, 1965; Morish, 1994). Although T_M is strongly dependent on Al content, the effect of Al contribution can be excluded because no Al-substitution exists in the present study.

In particular, grain morphology is an important factor in controlling the T_M. Mitra et al. (2009) investigated several sets of

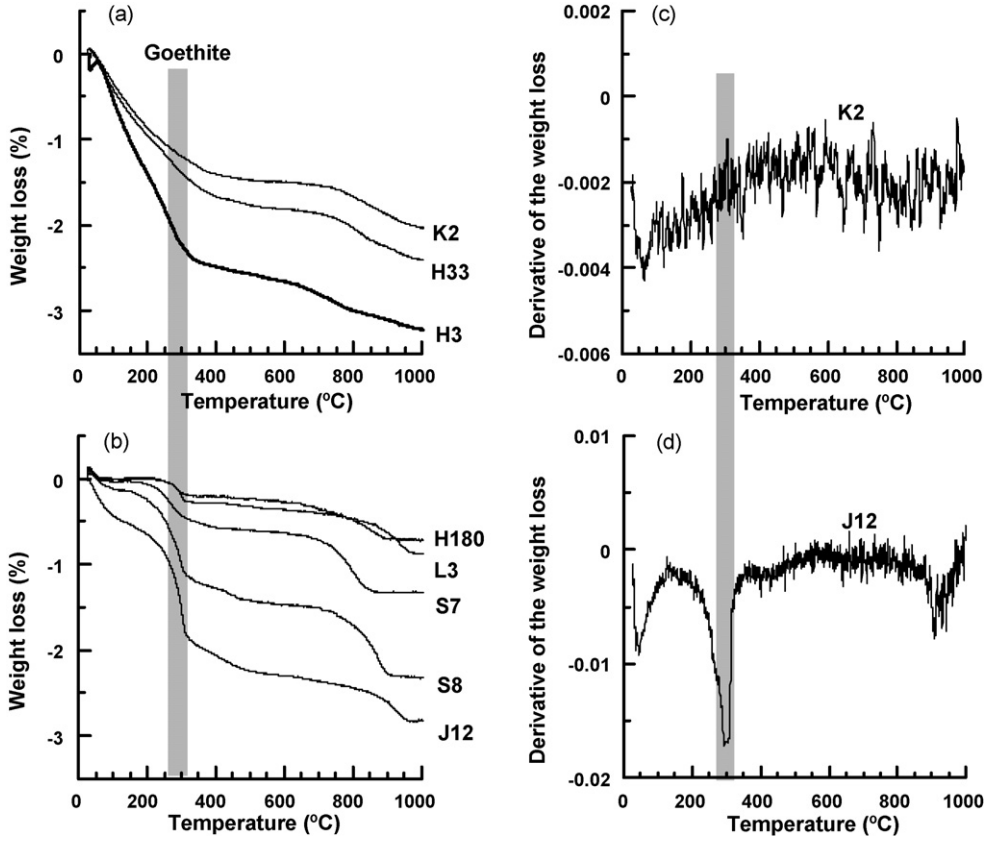

Fig. 4. The thermogravimetric spectra for the studied hematite samples. (a) Pseudocubic, and (b) platy and rhombohedral. The first-order derivatives of the thermogravimetric spectra for representative samples K2 and J12 are shown in (c) and (d), respectively. The gray bar marks the dominant weight loss due to goethite around 300 °C.

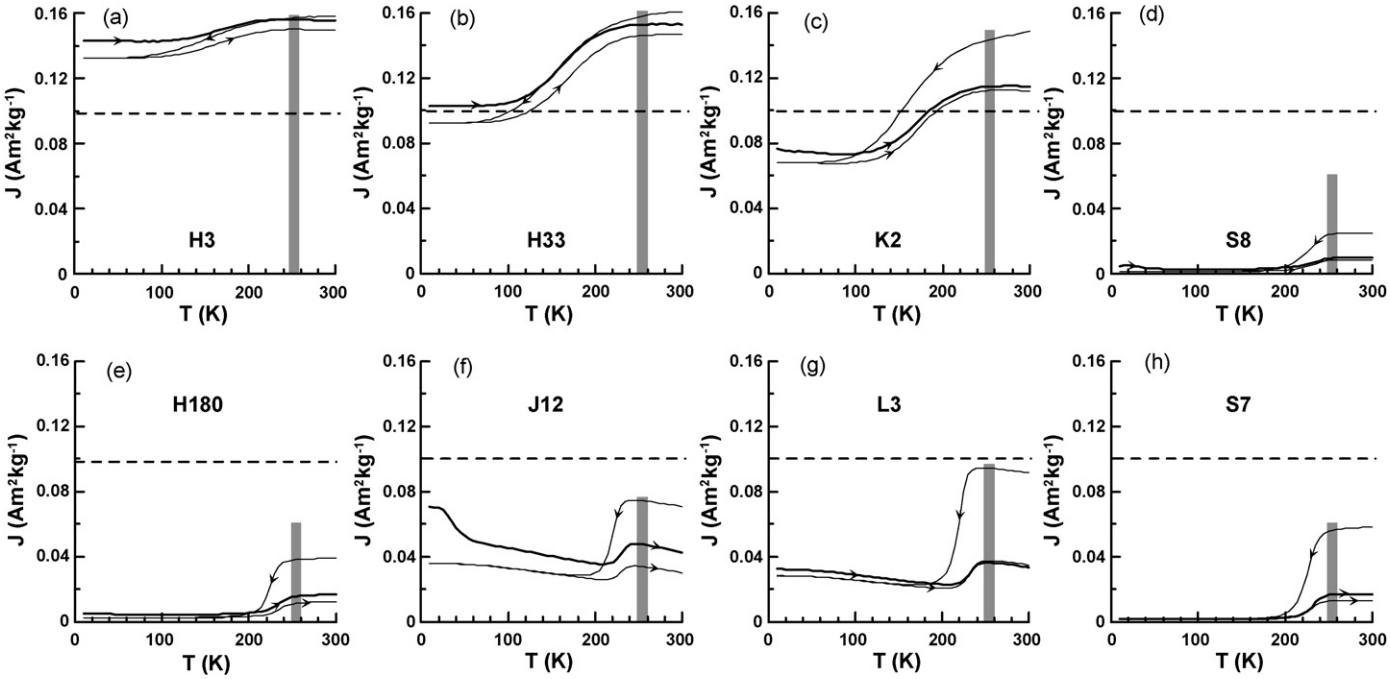

Fig. 5. Low-temperature cycle of IRM_{300K} (thin line) and warming curve (thick line) for IRM_{10K} for the studied hematite samples. The grey bars mark the standard Morin transition at about 250–260 K. The dashed horizontal lines ($J = 0.1\ Am^2\ kg^{-1}$) divide the samples into two groups. The magnetizations were normalized by the sample mass.

synthetic hematite samples of different morphology: ellipsoid, spindle, flattened, and rhombohedra. Among these samples, the ellipsoid hematite has the highest T_M value (251.4 K). In contrast, the T_M of rhombohedral hematite ranks the lowest (220.8 K). Nevertheless, these T_M values are much higher than that of the pseudocubic group examined in this study.

Thermogravimetric analyses showed that the pseudocubic samples displayed more OH capacity than the platy and rhombohedral samples (Fig. 4). In general, a higher OH capacity results in a cation vacancy (Wolska and Schwertmann, 1989), and thus strongly affects the magnetic properties of hematite particles.

As long as the present study is concerned, there are four important physical aspects that deserve highlighting. First, a highly depressed Morin transition characterizes the pseudocubic hematites. Such a transition at distributed temperature intervals resembles a reduced Verwey transition for SD magnetite. For such a case, the low-temperature behaviour is controlled dominantly by changes in the magnetic anisotropy constant (magnetoelastic anisotropy in the case of hematite). Decreases in the anisotropy constant, K_u, will result in decreases in coercivity $[B_c = 2K_u/(\mu_o \times M_s)]$ (where μ_o and M_s are the vacuum permeability and the saturation magnetization, resepctively), and thus the temperature-dependency of the B_c curve can also be used to define the Morin transition (Fig. 7). In contrast, the platy and rhombohedral samples have a well defined Morin transition, but still have a $T_M < 250$ K. The reduced T_M can also be attributed to the effects of vacancies or impurities.

Second, the saturation magnetization of hematite is also strongly linked to the vacancies. Theoretically, the M_s of antiferromagnetic minerals should be zero. However, the vacancies result in uncompensated spins, and hence strength M_s, which is about two orders of magnitude lower than that of magnetite. Table 2 shows that the Fe content for the pseudocubic sample is lower than that of the other samples except for sample J12, in which the presence of small amount of goethite results in underestimation of the hematite Fe content. However, the presence of more vacancies for the pseudocubic samples results in lower M_s is inconsistent with the theory above. An alternative mechanism could involve in the canted magnetization.

Third, morphology also strongly affects the magnetic properties of hematite. Platy hematite showed a much weaker magnetic coercivity. Considering its observed mean grain size, J12 must be dominated by SD properties. However, its hysteresis loop resembles a typical SP loop for magnetite. In fact, the platy hematite had an extremely smaller thickness of ~10–100 nm, comparable to a SP/SD threshold for hematite. In other words, for the platy samples, the thickness of the plate is one of the critical factors to determine the domain state of hematite.

Fourth, the vacancies further affect the room-temperature remanence memory. It has been well established that the initial remanence acquired at 300 K will be partially demagnetized upon the LTC treatment. The memory ratio of R_{SIRM} is defined as the ratio of the residual remanence after the LTC to the initial remanence at 300 K. Below the Morin transition, the lattice spins lie in the *c*-axis. As a result, the remanence acquired $< T_M$ simply represents the defect magnetization (M_{defect}). As such, it has been observed that SIRM memory R_{SIRM} is proportional to M_{defect} for natural multidomain hematite, commercial SD hematite, oxidation of magnetite (Fe_3O_4) to SD hematite, conversion of maghemite (Fe_2O_3) to SD hematite, and dehydration of goethite (FeOOH) to SD hematite (Özdemir and Dunlop, 2006). In the present study, a linear correlation ($R^2 = 0.86$) between R_{SIRM} and M_{defect} is also established (Fig. 9). However, the trend in this study is highly inclined towards the memory rather than the defect remanence compared to the study of Özdemir and Dunlop (2006) (Fig. 9). Such a distinctively different trend may result from the amount of stress exerted during sample preparation. For instance, samples used in the present study were synthesized from solution, known as to provide relatively stress-free environment (e.g. Heider et al., 1987; Dunlop and Argyle, 1997). Among these stress-free hematites, the largest stress was detected on pseudocubic morphologies where slight contamination of OH induced higher stress than the non-pseudocubic morphologies (Fig. 9).

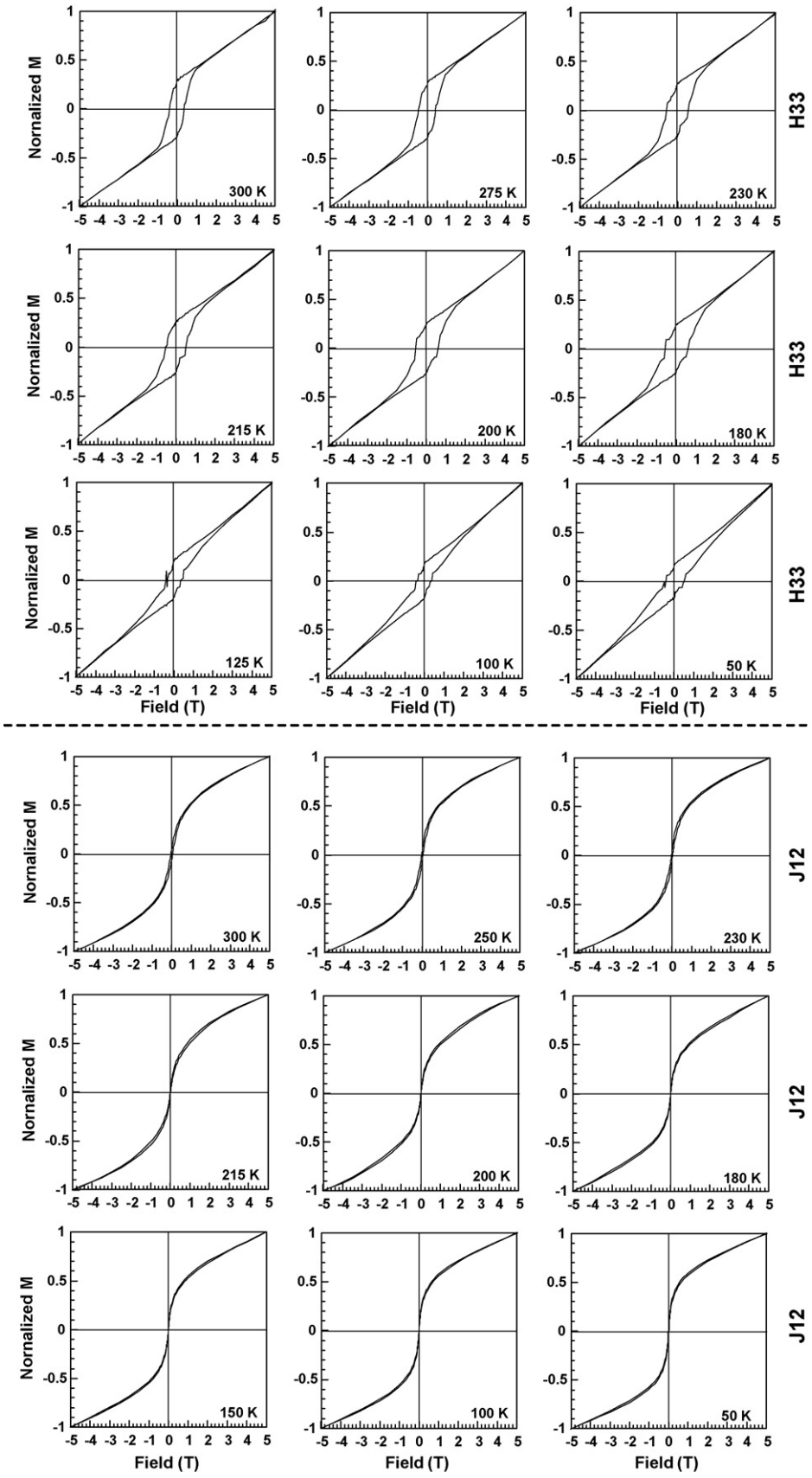

Fig. 6. Low-temperature-dependent hysteresis loops for the representative samples H33 (pseudocubic) and J12 (rhombohedral).

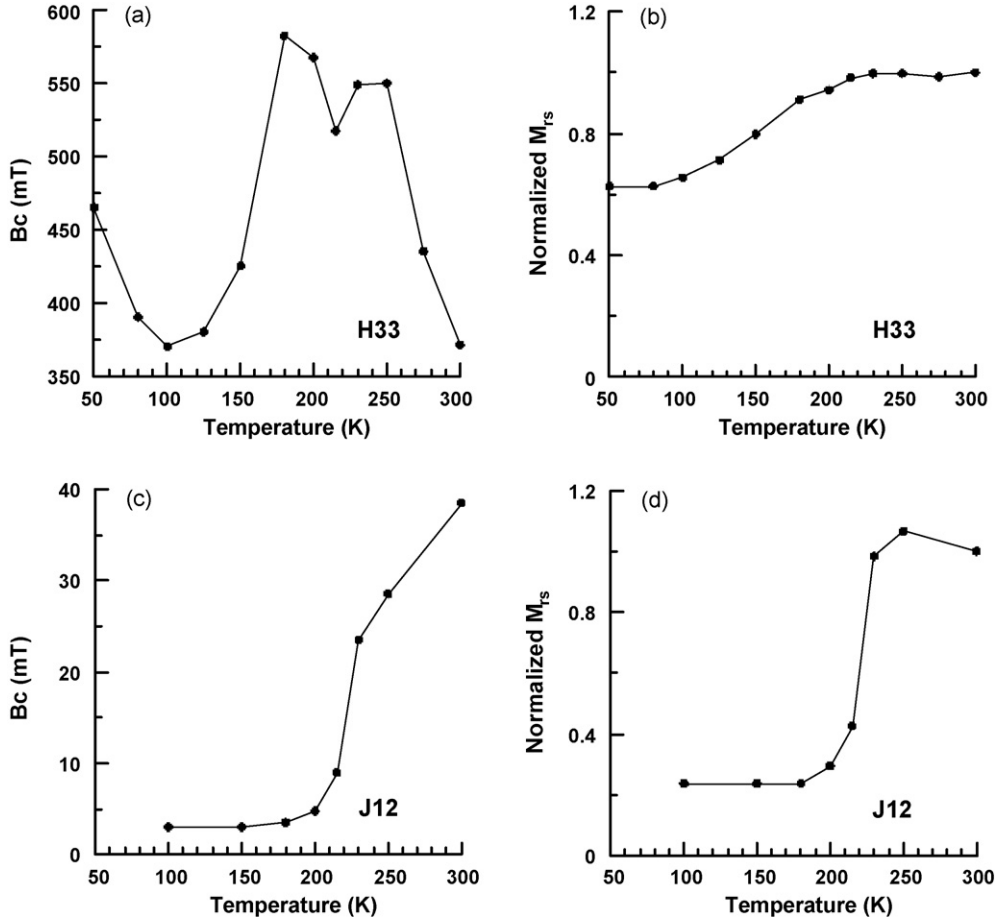

Fig. 7. Temperature-dependent hysteresis parameters for samples H33 (a and b), and J12 (c and d). M_{rs} is the remanence magnetization obtained directly from the hysteresis loop.

4.2. Magnetic coercivity for micron-sized hematite

Because of its weak magnetization, the coercivity of hematite is controlled dominantly by the magnetoelastic anisotropy (Dunlop and Özdemir, 1997). It has been observed that the coercivity of hematite depends on the grain size (Kletetschka and Wasilewski, 2002), annealing (by implication stress) (Dekkers, 1988), and the degree of cation substitution (or vacancies) (Wells et al., 1999; Roberts et al., 2006; Liu et al., 2007). The volume dependence of magnetic coercivity for hematite was first documented by Chevallier and Mathieu (1943). Such grain-size dependence was later extended to larger grains (Kletetschka and Wasilewski, 2002). Unlike magnetite, the SD/PSD threshold in hematite was only about 50–100 nm, coercivity steadily increasing from several tens of mT for 1–2 μm particles up to about 150 mT for ~20 μm particles and then decreasing to the background value when the grain size further increased from ~100 μm to 1 mm. By contrast, de Boer et al. (2001) found that the coercivity of hematite increased with decreasing grain size and reached a maximum (~470 mT) for the fine (<1 μm) fraction.

Annealing also strongly affected the coercivity of hematite. Dekkers (1988) found that after annealing, hematite samples can increase its coercivity by about several hundreds of mT. In addition, Liu et al. (2007) and Roberts et al. (2006) found that the coercivity of fine-grained hematite (several hundreds of nm) is strongly affected by aluminous substitution. With increasing degree of Al-substitution, the coercivity of hematite steadily and non-linearly increased from several tens of mT for pure hematite up to about several hundreds of mT for Al-substituted samples (with the maximum Al-substitution of ~14 mol%). Wells et al. (1999) proposed that Al-substitution in hematite results in the development of lattice defects and an increase in the number of the particle crystallites by shrinking the mean crystallite dimensions. Hence, Al-substitution can stabilize the domain and increase coercivity.

For any magnetic minerals, coercivity originates from shape, magnetoelastic, and/or magnetocrystalline anisotropies. Özdemir et al. (2002) systematically investigated the variations in coercivity of magnetite at low temperature. For a large (1.3 mm) magnetite crystal controlled dominantly by magnetocrystalline anisotropy, coercivity gradually decreased upon cooling and reached a small value at T_i, where K_1 becomes zero. Nearly identical signature was duplicated in J12, strongly indicating a dominant magnetocrystalline anisotropy (Fig. 7).

In contrast, sample H33 showed a more complicated pattern with a minimum coercivity of ~350 mT at 100 K (Fig. 7). Indeed, the entire pattern can be interpreted as a mixture of a steadily increasing trend upon cooling and a drop when crossing the Morin transition between 100 and ~170 K. The decrease in coercivity upon cooling crossing the Morin transition can be reasonably attributed to the magnetocrystalline anisotropy as in J12 (Fig. 7). The increasing trend in coercivity upon cooling below 100 K may result from the magnetoelastic anisotropy, caused by vacancies associated with the OH groups in pseudocubic morphology.

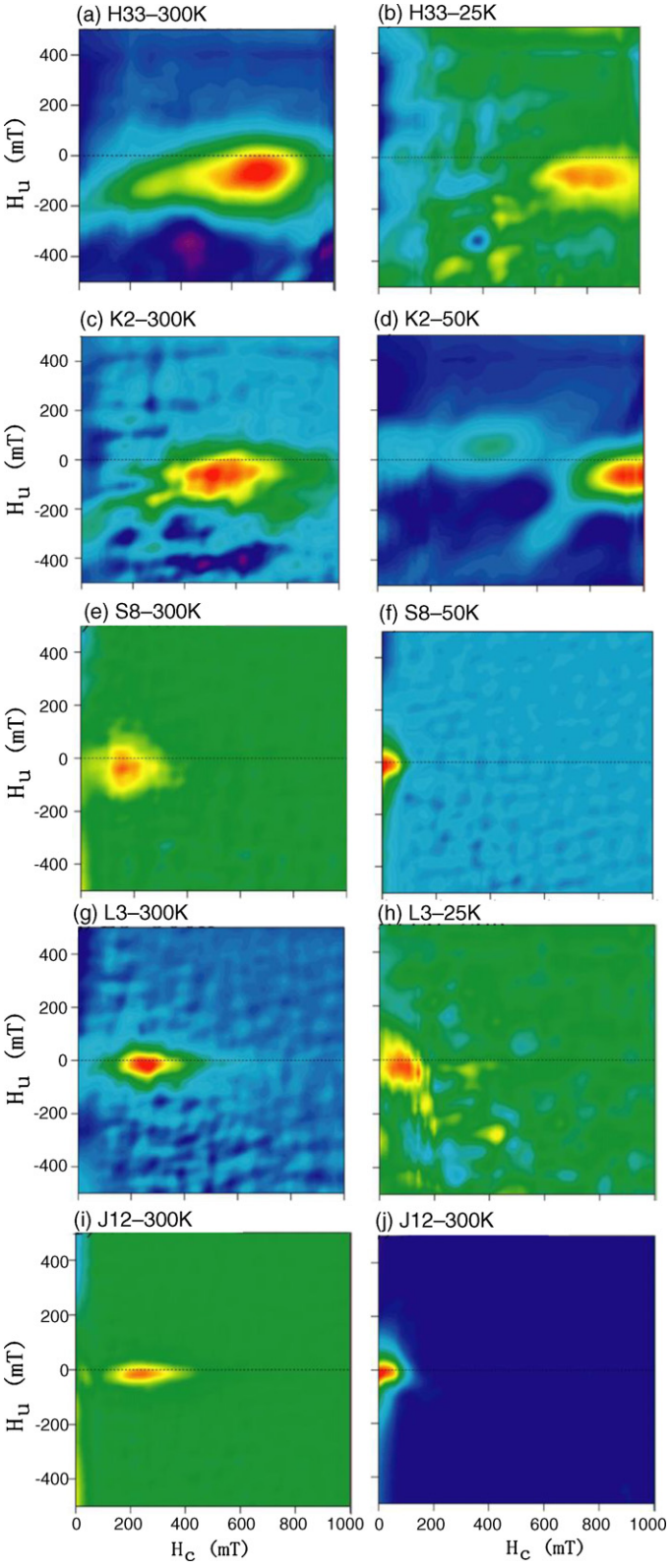

Fig. 8. FORC diagrams for two groups of hematite samples measured at room temperature and low temperatures.

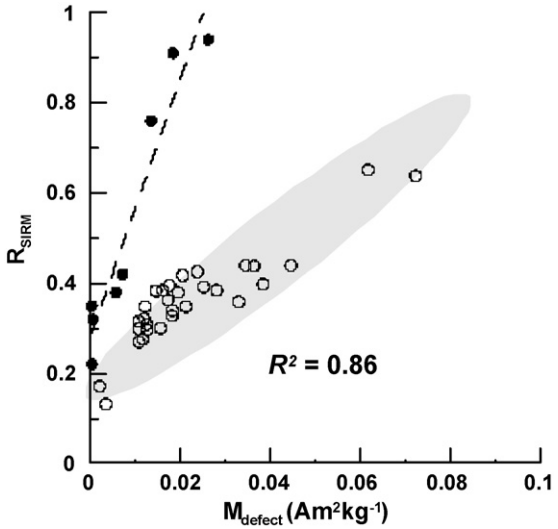

Fig. 9. Plot of the memory ratio R_{SIRM} versus the defect magnetization M_{defect} (the value of 300-K SIRM, measured at 20 K). The solid and open circles indicate data from this study and from Özdemir and Dunlop (2006), respectively. The dashed line indicates the linear trend (R^2 = 0.86) for the data from this study. The dashed region indicates the background trend for data from Özdemir and Dunlop (2006).

This interpretation can reasonably account for the FORC diagram patterns. For the pseudocubic samples (H33 and K2) (which possess more vacancies), magnetoelastic anisotropy dominates the coercivity, and thus at low temperatures, its CPFD is shifted towards higher values. In contrast, for the platy samples (less vacancies), the dominant factor is magnetocrystalline anisotropy and thus coercivity undergoes reduction because K_1 gradually decreases.

4.3. Further implications of the grain morphology

In nature, morphology of hematite crystal represents its growing environment. For example, Rösler (1983) found that the thickness of hematite plates formed under hydrothermal conditions reflect temperature conditions. If so, the morphologic difference in hematite is potentially useful in environmental application. Hematite is extremely important because it carries highly stable NRM and is much resistant to later alteration or metamorphism than magnetite. In fact, identifying the sources of NRM for hematite-bearing rocks is often required because they carry different types of NRM. For example, detrital hematite carries primary depositional remanence magnetization (DRM), whereas secondary hematite carries chemical remanence magnetization (CRM), which can contaminate DRM and thus complicate the interpretation of paleomagnetic results. In addition, presence of hematite can provide pivotal clue for the evolution of Martian lithosphere (Catling and Moore, 2003; Baldridge and Calvin, 2004; Scott and Fuller, 2004).

The simplest yet useful proposition by Rendón and Serna (1981) is useful to determine the shape of hematite on the basis of the IR adsorption spectra. Similar interpretations in Iglesias and Serna (1985) and in this study confirm that the IR adsorption is in principle valid for morphology distinction. In the future, a combination of magnetic and mineralogical characterization will be recommended to discriminate hematite of different origins.

5. Conclusions

The main conclusions of the present study are:

(1) The micron-sized hematite samples examined in this study can be divided into three groups in terms of their crystal morphology as pseudocubic, platy, and rhombohedral. Because these three groups of hematite were synthesized in different environments, and thus their intrinsic micro-structures were different, they exhibited different magnetic properties.

(2) Observed coercivities range from several tens of mT (non-pseudocubic) to several hundreds of mT (pseudocubic). Such morphology dependence of magnetic coercivity results from a dominant magnetoelastic anisotropy in pseudocubic grains due to the presence of vacancies caused by the incorporation of OH in the crystal structure.

(3) The Morin transition is also directly related to vacancies. The higher degree of OH incorporation in the pseudocubic crystal structure yields more vacancies, and thus smeared the Morin transition. A rather sharp (but shifted towards lower temperatures than expected) Morin transition is observed only for non-pseudocubic grains.

(4) The shape factor $G_{\perp}$ is consistent with the morphology of hematite. This study confirms that $G_{\perp}$ is valid in distinguishing crystal shape even for micron-sized hematites, and thus could be a potential proxy to discriminate hematite of different origins.

Acknowledgements

This study was supported by the National Natural Science Foundation of China (grants 40974036 and 40821091), the CAS/SAFEA International Partnership Program for Creative Research Teams, and the Chinese Academy of Sciences. Q. Liu acknowledges further supports from the 100-talent Program of the Chinese Academy of Sciences. J. Torrent and V. Barrón were partly supported by Spain's Ministerio de Educación y Ciencia, Project AGL2006–10927, and the European Regional Development Fund.

References

Ayyub, P., Multani, M., Barma, M., Palkar, V.R., Vijayaraghavan, R., 1988. Size-induced structural phase transitions and hyperfine properties of microcrystalline Fe_2O_3. J. Phys. C: Solid State Phys. 21, 2229, doi:10.1088/0022-3719/21/11/014.

Baldridge, A.M., Calvin, W.M., 2004. Hydration state of the Martian coarse-grained hematite exposures: implications for their origin and evolution. J. Geophys. Res. 109, E04S90, doi:10.1029/2003JE002066.

Bando, M., Kiyama, Y., Yamamoto, N., Takada, T., Shinjo, T., Takaki, H., 1965. Magnetic properties of α-Fe_2O_3 fine particles. J. Phys. Soc. Jpn. 20, 2086.

Banerjee, S.K., 1971. New grain size limits for paleomagnetic stability in hematite. Nat. Phys. Sci. 232, 15–16.

Barrón, V., Rendón, J.L., Torrent, J., Serna, C.J., 1984. Relation of infrared, crystallochemical, and morphological properties of Al-substituted hematites. Clay Clay Miner. 32, 475–479.

Barrón, V., Herruzo, M., Torrent, J., 1988. Phosphate adsorption by aluminous hematites of different shapes. Soil. Soc. Am. J. 52, 647–651.

Catling, D.C., Moore, J.M., 2003. The nature of coarse-grained crystalline hematite and its implications for the early environment of Mars. Icarus 165, 277–300.

Chevallier, R., Mathieu, S., 1943. Proprietes magnetiques des poudres hematite-influence des dimensions des grains. Ann. Phys. 18, 258–288.

Dankers, P.H.M., 1981. Relationship between the median destructive field and remanence coercivity forces for dispersed magnetite, titanomagnetite and hematite. Geophys. J. Roy. Astron. Soc. 64, 447–461.

de Boer, C.B., Mullender, T.A.T., Dekkers, M.J., 2001. Low-temperature behaviour of haematite: susceptibility and magnetization increase on cycling through the Morin transition. Geophys. J. Int. 146, 201–216.

de Boer, C.B., Dekkers, M.J., 1998. Thermomagnetic behaviour of hematite and goethite as a function of grain size in various nonsaturating magnetic fields. Geophys. J. Int. 133, 541–552.

de Grave, E., Bowen, L.H., Weed, S.B., 1982. Mössbauer study of aluminum-substituted hematites. J. Magn. Magn. Mater. 27, 98–108.

de Grave, E., Chamebaere, D.G., Bowen, L.H., 1983. Nature of the Morin transition in Al-substituted hematite. J. Magn. Magn. Mater. 30, 349–354.

Dekkers, M.J., 1988. Some rockmagnetic parameters for natural goethite, pyrrhotite and fine-grained hematite. (PhD Thesis, University of Utrecht). Geologica Ultraiectina, 51, 231 pp.

Dekkers, M.J., Linssen, J.H., 1989. Rock magnetic properties of fine-grained natural low-temperature hematite with reference to remanence acquisition mechanisms in red beds. Geophys. J. Int. 99, 1–18.

Dunlop, D.J., Argyle, K.S., 1997. Thermoremanence, anhysteretic remanence and susceptibility of submicron magnetites: nonlinear field dependence and variation with grain size. J. Geophys. Res. 102, 20199–20210.

Dunlop, D.J., Kletetschka, G., 2001. Multidomain hematite: a source of planetary magnetic anomalies? Geophys. Res. Lett. 28, 3345–3348.

Dunlop, D.J., Özdemir, Ö., 1997. Rock Magnetism: Fundamentals and Frontiers. Cambridge Press, p. 573.

Flanders, P.J., Remeika, J.P., 1965. Magnetic properties of hematite single crystals. Philos. Mag. 11, 1271–1288.

Flanders, P.J., Schuele, W.J., 1964. Temperature dependent magnetic properties of hematite single crystals. In: Proc. Int. Conf. Magnetism, Nottingham, pp. 594–596.

Hamada, S., Matijević, E., 1982. Formation of monodispersed colloidal pseudocubic haematite particles in ethanol + water solutions. J. Chem. Soc. Faraday Trans. 1, 2147–2156.

Heider, F., Dunlop, D.J., Sugiura, N., 1987. Magnetic properties of hydrothermally re-crystallized magnetite crystals. Science 236, 1287–1290.

Iglesias, J.E., Serna, C.J., 1985. The IR spectra of hematite-type compounds with different particle shapes. Miner. Petrogr. Acta 29, 363–370.

Kletetschka, G., Wasilewski, P.J., 2002. Grain size limit for SD hematite. Phys. Earth Planet. Inter. 129, 173–179.

Kletetschka, G., Wasilewski, P.J., Taylor, P.T., 2000. Hematite versus magnetite as the signature for planetary magnetic anomalies. Phys. Earth Planet. Inter. 119, 259–267.

Kraus, W., Nolze, G., 1996. POWDER CELL (a program for the representation and manipulation of crystal structures and calculation of the resulting X-ray powder patterns). J. Appl. Crystallogr. 29, 301–303.

Larrasoaña, J.C., Roberts, A.P., Rohling, E.J., Winklhofer, M., Wehausen, R., 2003. Three million years of monsoon variability over the northern Sahara. Clim. Dyn. 21, 689–698.

Larrasoaña, J.C., Roberts, A.P., Hayes, A., Wehausen, R., Rohling, E.J., 2006. Detecting missing beats in the Mediterranean climate rhythm from magnetic identification of oxidized sapropels (Ocean Drilling Program Leg 160). Phys. Earth Planet. Inter. 156, 283–293.

Liu, Q.S., Roberts, A.P., Torrent, J., Horng, C.-S., Larrasoaña, J.C., 2007. What do the HIRM and S-ratio really measure in environmental magnetism? Geochem. Geophys. Geosys. 8, Q09011, doi:10.1029/2007GC001717.

Maher, B.A., Dennis, P.F., 2001. Evidence against dust-mediated control of glacial–interglacial changes in atmosphere CO_2. Nature 411, 176–180.

Mitra, S., Das, S., Basu, S., Sahu, P., Mandal, K., 2009. Shape- and field-dependent Morin transitions in structured α-Fe_2O_3. J. Magn. Magn. Mater. 321, 2925–2931.

Morin, F.J., 1950. Magnetic susceptibility of α-Fe_2O_3 and Fe_2O_3 with added titanium. Phys. Rev. 78, 819–820.

Morish, A.H., 1994. Canted Antiferromagnetism: Hematite. World Scientific, Singapore.

Muench, G.J., Arajs, S., Matijevic, E., 1985. The Morin transition in small α-Fe_2O_3 particles. Phys. State Solid (a) 92, 187–192.

Özdemir, Ö., Dunlop, D.J., 2006. Magnetic memory and coupling between spin-canted and defect magnetism in hematite. J. Geophys. Res. 111, B12S03, doi:10.1029/2006JB004555.

Özdemir, Ö., Dunlop, D.J., Moskowitz, B.M., 2002. Changes in remanence, coercivity and domain state at low temperature in magnetite. Earth Planet. Sci. Lett. 194, 343–358.

Özdemir, Ö., Dunlop, D.J., 2005. Thermoremanent magnetization of multidomain hematite. J. Geophys. Res. 110, B09104, doi:10.1029/2005JB003820.

Pastrana, J.M., Hopstock, D.M., 1977. Magnetic properties of natural hematite and goethite. Trans. SME/AIME 262, 1–5.

Prasada, P.S.R., Shiva Prasada, K., Krishna Chaitany, V., Babua, E.V.S.S.K., Sreedharc, B., Ramana Murthyd, S., 2006. In situ FTIR study on the dehydration of natural goethite. J. Asian Earth Sci. 27, 503–511.

Rendón, J.L., Serna, C.J., 1981. IR spectra of powder hematite: effects of particle size and shape. Clay Miner. 16, 375–381.

Roberts, A.P., Liu, Q.S., Rowan, C.J., Chang, L., Carvallo, C., Torrent, J., Horng, C.S., 2006. Characterization of hematite (alpha-Fe_2O_3), goethite (alpha-FeOOH), greigite (Fe_3S_4), and pyrrhotite (Fe_7S_8) using first-order reversal curve diagrams. J. Geophys. Res. 111 (B12), B12S35, doi:10.1029/2006JB004715.

Rösler, H.J., 1983. Lehrbuch der Mineralogie. Verlag für Grundstoffindustrie, Leipzig, 832 pp.

Schwertmann, U., Cornell, R.M., 2000. Iron Oxides in the Laboratory, Preparation and Characterization. Wiley-VCH, Weinheim, 188 pp.

Schwertmann, U., Taylor, R.M., 1977. Iron oxides. In: Dixon, J.B., Weed, S.B. (Eds.), Minerals in Soil Environments, Soil Science Society of America, Madison, WI, pp. 145–180.

Scott, E.R.D., Fuller, M., 2004. A possible source for the Martian crustal magnetic field. Earth Planet. Sci. Lett. 220, 83–90.

Sugimoto, T., Muramatsu, A., Sakata, K., Shindo, D., 1993. Characterization of hematites particles of different shapes. J. Colloid Interface Sci. 158, 420–428.

Sunagawa, I., Flanders, P.J., 1965. Structural and magnetic studies in hematite single crystals. Philos. Mag. 11, 747–761.

Tauxe, L., Kent, D.V., 1984. Properties of a detrital remanence carried by hematite from study of modern river deposits and laboratory redeposition experiments. Geophys. J. Roy. Astron. Soc. 76, 543–561.

Thompson, R., Oldfield, F., 1986. Environmental Magnetism. Allen & Unwin, London, 227 pp.

Torrent, J., Schwertmann, U., 1987. Influence of hematite on the colour of red beds. J. Sed. Petrol. 57, 682–686.

Van de Hulst, H.C., 1957. Light Scattering by Small Particles. John Wiley & Sons, New York, pp. 70–72.

Verwey, E.J.W., 1939. Electron conduction of magnetite (Fe_3O_4) and its transition point at low temperatures. Nature 144, 327–328.

Wells, M.A., Fitzpatrick, R.W., Gilkes, R.J., Dobson, J., 1999. Magnetic properties of metal-substituted haematite. Geophys. J. Int. 138, 571–580.
Wolska, E., 1981. The structure of hydrohematite. Kristallogr. Z. 154, 69–75.
Wolska, E., Schwertmann, U., 1989. Nonstoichiometric structures during dehydroxylation of goethite. Kristallogr. Z. 189, 223–237.
Yamazaki, T., Ioka, N., 1997. Environmental rock-magnetism of pelagic clay: implications for Asian eolian input to the North Pacific since the Pliocene. Paleoceanography 12, 111–124.
Zhao, Y.M., Dunnill, C.W., Zhu, Y.Q., Gregory, D.H., Kockenberger, W., Li, Y.H., Hu, W.B., Ahmad, I., McCartney, D.G., 2007. Low-temperature magnetic properties of hematite nanorods. Chem. Mater. 19, 916–921.
Zysler, R.D., Vasquez-Mansilla, M., Arciprete, C., Dimitrijewits, M., Rodriguez-Sierra, D., Saragovi, C., 2001. Structure and magnetic properties of thermally treated nanohematite. J. Magn. Magn. Mater. 224, 39–48.